JOURNAL OF AIRCRAFT
Vol. 31, No. 4, July–Aug. 1994

Unsteady Vortex Dynamics and Surface Pressure Topologies on a Finite Pitching Wing

Scott J. Schreck* and Hank E. Helin†
U.S. Air Force Academy, Colorado Springs, Colorado 80840

A straight wing having an NACA 0015 cross section and rectangular planform was attached to a circular splitter plate. This configuration was pitched at a constant rate to angles exceeding the static stall angle. The unsteady, vortex-dominated flow that developed over the wing and splitter plate was characterized in detail using surface pressure measurements and flow visualization. Both types of data showed that the leading-edge vortex underwent profound three-dimensional alterations to cross section and convection over the entire wing span. These changes in leading-edge vortex structure and kinematics were correlated with prominent spanwise variations in force coefficients. When appropriately dissected, visualization results and pressure data suggested physical mechanisms to account for these three-dimensional variations in unsteady forces and surface pressures.

Nomenclature

C_n = normal force coefficient
c = wing chord length, cm
c_p = pressure coefficient
LE = leading edge
Re_c = chord Reynolds number
s = wing span length, cm
t = time, s
t_{nd} = nondimensional time, tU_∞/c
U_∞ = test section velocity, m/s
x = chordwise distance from leading edge
y = spanwise distance from splitter plate
α = instantaneous angle of attack, deg
$\dot{\alpha}$ = pitch rate, rad/s
α^+ = nondimensional pitch rate, $c\dot{\alpha}/U_\infty$

Introduction

THREE-DIMENSIONAL dynamically separated flows continue to be intensely studied. Energetic large-scale vortical structures are generated and transiently reside on wings dynamically pitched through the static stall angle of attack. These vortical structures radically alter the pressure distributions on a wing, thus producing greatly amplified aerodynamic forces and moments. If thoroughly understood and properly controlled, three-dimensional dynamically separated flows have the potential to confer dramatic performance enhancements upon future aircraft.

Flow visualization studies have documented the morphology of portions of three-dimensional unsteady flows elicited by pitching wings.[1–6] These studies concentrated attention on the prominent leading-edge and wingtip vortices, and successfully constructed simplistic physical models based upon vorticity conservation to explain vortex anchoring and tapering near the wingtip. Fewer investigations have employed surface pressure measurements to characterize three-dimensional unsteady flowfield development on pitching wings.[7,8] These studies found unsteady spanwise pressure distributions to be augmented near the wingtip in comparison to the steady spanwise distribution.

Unsteady flows near wing-wall junctures have been shown to be as complex as those near the wingtip. Shih[9] examined the dynamically separated flowfield over a wing spanning a test section in which the flow speed varied sinusoidally. Velocity surveys revealed strong spanwise three-dimensionality that exhibited convective behavior suggesting the presence of separated vortical eddies. Horner and colleagues[10] employed flow visualization to show that the unsteady flow near the juncture between a fixed wall and a pitching wing was two dimensional immediately following leading-edge vortex initiation. However, as the vortex convected along the wing chord, the vortex arched away from the wing surface near center span, and symmetrical counter-rotating cells formed on the wing surface. Three-dimensional disruptions to the leading-edge vortex were explained with a model that relied upon mutual induction between orthogonal vortex segments.

Schreck and coworkers[11] and Klinge et al.[12] investigated the dynamically separated flow near the juncture between a wing and splitter plate undergoing constant rate and sinusoidal pitching, respectively. Both experiments measured unsteady surface pressures, enabling unambiguous characterization of leading-edge vortex convection and quantification of time-dependent normal forces. In the juncture region, the leading-edge vortex convected at a faster velocity and unsteady stall occurred earlier. Preliminary vorticity dynamics models were postulated to explain alterations to leading-edge vortex convection near the juncture.

The current investigation combines quantitative surface pressure topologies with flow visualization at identical nondimensional pitch rates and closely matched Reynolds numbers. This approach allows the presence and behavior of visualized vortex structures to be unambiguously confirmed by distinctive pressure signatures. This methodology also enables vorticity generation sites and rates to be inferred using surface pressure topologies. Thus, vorticity not aggregated into vortical structures can also be accounted for. Both flow visualization and surface pressure measurements show significant spanwise variability in the unsteady flowfield development. To account for this variability, a model is hypothesized for the three-dimensional unsteady flowfield on the wing-splitter plate configuration.

Experimental Methods

Surface Pressure Measurement

Surface pressure measurements were performed in the Frank J. Seiler 0.91- × 0.91-m low-speed wind tunnel located at the

Presented as Paper 93-0435 at the AIAA 31st Aerospace Sciences Meeting and Exhibit, Reno, NV, Jan. 11–14, 1993; received April 21, 1993; revision received Oct. 14, 1993; accepted for publication Oct. 30, 1993.

*Unsteady Aerodynamics Task Manager, Frank J. Seiler Research Laboratory, 2354 Vandenberg Dr., Ste. 6H79. Member AIAA.

†Assistant Professor, Department of Aeronautics, 2410 Faculty Dr., Ste. 106. Senior Member AIAA.

U.S. Air Force Academy. A rectangular planform wing with 15.24-cm chord length was fabricated from hollow aluminum NACA 0015 airfoil stock. The basic wing was 29.10 cm long and was equipped with a fitting on the outboard end that permitted arbitrary length extensions to be added. Fifteen miniature pressure transducers were installed inside the hollow basic wing model. These transducers were close coupled to the wing surface through pressure ports located along the chord line, 3.05 cm inboard of the basic wing end. Pressure transducer signals were low-pass filtered (300 Hz cutoff) and amplified by a gain of 500. The resulting signals were then sampled and digitized by the data acquisition system.

A circular aluminum splitter plate, 30.48 cm in diam and 0.64 cm thick, was machined to a sharp edge around the plate perimeter. The splitter plate had an NACA 0015 cutout centered in it, which allowed it to slide onto the wing and be positioned at arbitrary span locations. To effectively move the pressure ports along the wing span, the splitter plate was first positioned at the desired distance from the pressure ports. Then, a tip extension of the correct length was added to the basic wing, bringing the span length to 30.48 cm and maintaining aspect ratio constant at 2.0. The chordwise row of pressure ports was successively moved to 11 span locations, effectively distributing pressure ports over the wing surface as shown in Fig. 1. All 11 tip extensions used in these experiments terminated in a square tip.

In Fig. 1, spanwise pressure port locations range from 0.0 to 0.80 span outboard of the splitter plate. Chordwise pressure port locations range from -0.90 to 0.90 chord, with 0.0 chord corresponding to the wing leading edge. Positive chord values denote the wing upper surface, whereas negative chord signifies the lower surface. Unsteady surface pressures measured at these port locations were contour-plotted using a linear interpolation between adjacent grid points in both the chordwise and spanwise directions.

Model pitching was driven by a 3.5-hp synchronous stepper motor. The wing-splitter plate combination was mounted on a steel shaft 2.86 cm in diam that was connected to the stepper motor through a gear linkage having a 4:1 reduction ratio. The independent variables explored in the surface pressure experiments included nondimensional pitch rates 0.05, 0.10, and 0.20, as well as spanwise pressure port locations 0.0, 0.05, 0.10, 0.15, 0.25, 0.375, 0.50, 0.625, 0.70, 0.75, and 0.80 span outboard of the splitter plate. Wing pitch axis was located at 0.25 chord for the experimental range of nondimensional pitch rate, and at 0.33 chord for nondimensional pitch rate 0.10. For each parameter combination, 20 consecutive wing pitch motions were sampled and ensemble-averaged. Test section velocity was held constant at 9.14 m/s, corresponding to a chord Reynolds number of 6.9×10^4.

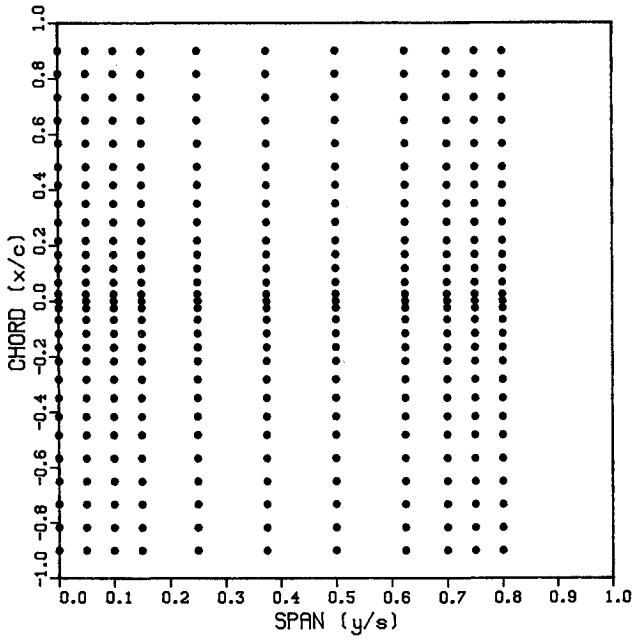

Fig. 1 Effective distribution of pressure port locations over the wing planform.

Flow Visualization

Flow visualization was performed in the U.S. Air Force Academy 0.51- × 0.38-m water tunnel. Dimensions of the flow visualization wing-splitter plate model were identical to those of the surface pressure measurement model. A 0.13-mm-wide slot was cut through the leading edge of the flow visualization wing along the entire wing span. This slot allowed dye to flow from the hollow wing interior to the wing exterior. Both wing and splitter plate were painted white to maximize visibility of the dark blue dye. Dye was injected directly into the boundary layer, visualizing the vorticity in the unsteady flowfield.

The wing-splitter plate model used for flow visualization was mounted on a steel shaft 0.95 cm in diam. The model was pitched at constant rate by a 24-V dc gear motor that was connected to the model through a gear linkage having a 5:1 reduction ratio. The visualized flowfield was illuminated by two 100-W incandescent lamps. Flow visualization images were recorded from the wing planform perspective at 30 frames/s by a VHS video camera.

Water tunnel flow visualization was performed at a test section velocity of 0.44 m/s and a water temperature of 12.8°C. This yielded a chord Reynolds number of 5.6×10^4 that corresponded closely to that of 6.9×10^4 for wind-tunnel surface pressure measurements. Flow was visualized for nondimensional pitch rates of 0.05, 0.10, and 0.20, using pitch axis locations of 0.25 and 0.33 chord. Volume coefficient of injection[13] out of the leading-edge slot was modest, being 0.01.

Results

Pitching the wing-splitter plate configuration beyond static stall elicited dramatic three-dimensional modifications to leading-edge vortex structure. Visualized leading-edge vortex locations and structures correlated closely with minima in the surface pressure topologies. Three-dimensional modifications to the leading-edge vortex and correlation with surface pressure topologies persisted throughout the experimental range. Leading-edge vortex kinematics at all span locations were also well-correlated with spanwise normal force loading.

Angle-of-attack angle histories for the three measured nondimensional pitch rates of 0.05, 0.10, and 0.20 are shown in Fig. 2. All three histories begin at 0.0 deg and end at 60.0 deg. The beginning of these histories coincides with the inception of surface pressure data acquisition. Thus, the plots in Fig. 2 can be used in conjunction with subsequent plots to convert nondimensional time to instantaneous wing angle of attack. For surface pressure measurements, the wing was pitched at a constant rate from 0.0 to 60.0 deg to collect upper

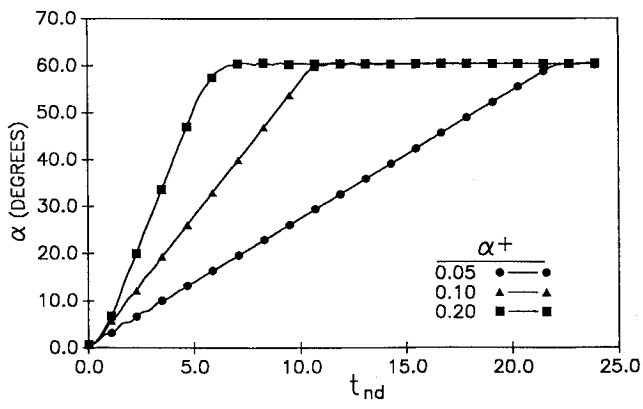

Fig. 2 Angle of attack histories for the experimental range of α^+.

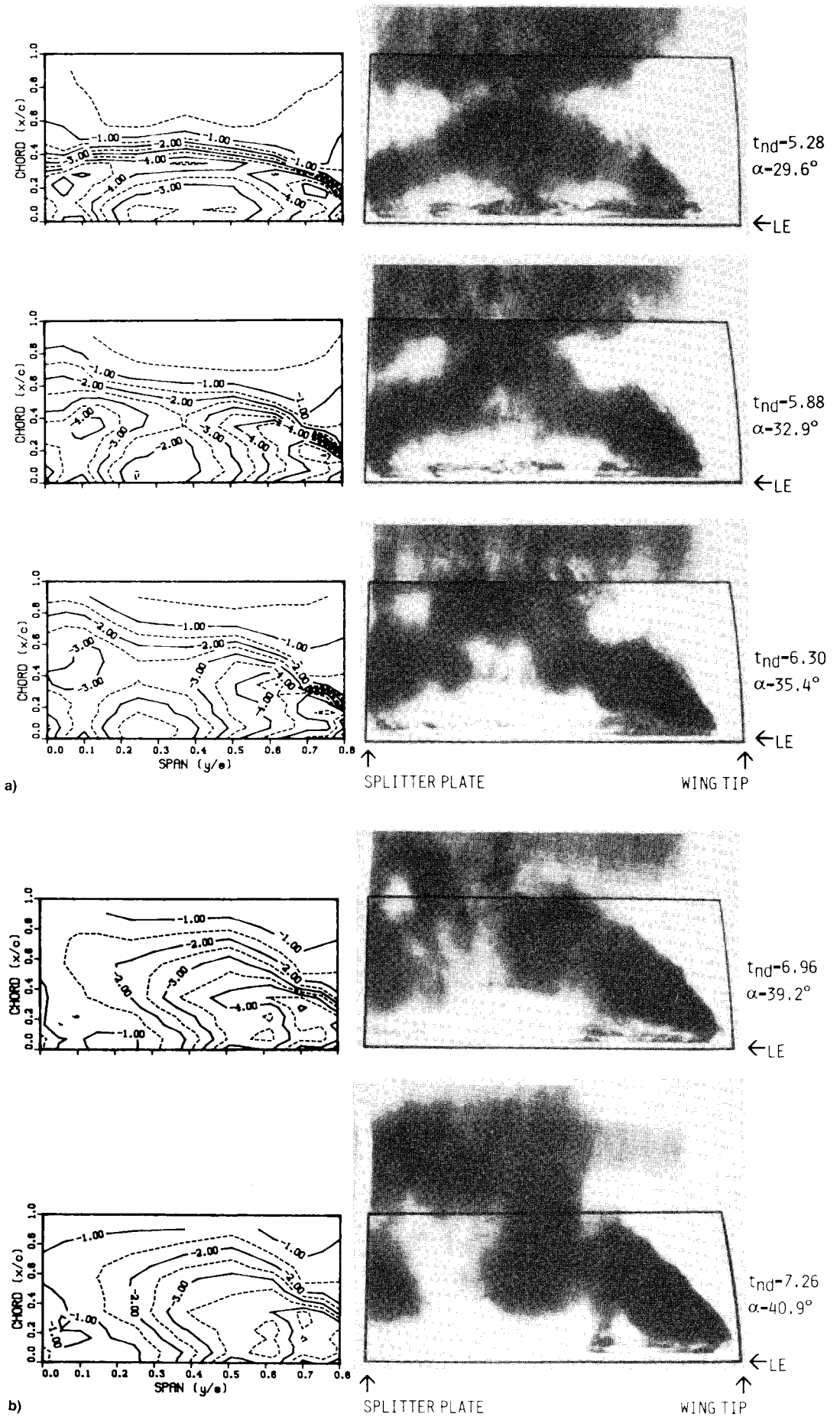

Fig. 3 Surface pressure topologies and corresponding flow visualizations for $\alpha^+ = 0.10$ and pitch axis at $0.33c$, for t_{nd} = a) 5.28, 5.88, and 6.30 and b) 6.96 and 7.26.

surface data, and from 0 deg to −60.0 deg to acquire lower surface data. It should be noted that none of the angle-of-attack histories exhibits prominent nonlinearity or suffers from appreciable acceleration or deceleration transients.

Vortex Structure and Surface Pressure Topologies

Figure 3 shows a representative series of five surface pressure coefficient topologies and corresponding dye flow visualization photographs. Nondimensional pitch rate was 0.10, and the wing was pitched about 0.33 chord. Note that surface pressure topologies extend 0.80 span from the splitter plate, whereas flow visualization shows the entire wing span. For clarity, the wing planform has been outlined in the visualization photographs. Lower surface pressure topologies were characterized by mild two-dimensional pressure gradients that underwent limited temporal evolution. Thus, lower surface data will not be presented here.

The frame 1 (t_{nd} = 5.28) surface pressure topology in Fig. 3 is dominated by an arc-shaped suction ridge that begins near the intersection of the splitter plate and wing leading edge. The suction ridge proceeds outboard across the wing span, curves back to 0.33 chord at center span, and again approaches the leading-edge 0.80 span outboard of the splitter plate. Suction ridge position corresponds closely to the upstream boundary of the visualized leading-edge vortex. Near the splitter plate and wingtip, at 0.18 chord, prominent localized suction peaks disrupt suction ridge uniformity. Both suction peaks lie close to portions of the vortex that exhibit pronounced flexure in the visualization. Upstream of the suction ridge, two wedge-shaped contours, 0.25 and 0.50 span from the splitter plate and just behind the leading edge, denote pressure maxima that lie on either side of a low-pressure region. This low-pressure region corresponds to a chordwise dye streak that connects the wing leading edge and the vortex upstream boundary.

In frame 2 (t_{nd} = 5.88), the suction ridge remains evident in the surface pressure topology. The inboard end of the suction ridge is still located near the intersection of the splitter plate and wing leading edge, and the outboard end still terminates near the wing leading edge. Visualization is consistent, showing the inboard and outboard ends of the vortex still located near the leading edge. Suction ridge magnitude has been substantially diminished near center span, where visualization indicates that the leading-edge vortex has arched up and away from the wing surface. Two local suction peaks are still present in the surface pressure topology. The inboard peak has moved downstream and is located at 0.36 chord, while the outboard suction peak remains at 0.18 chord. Suction peak locations lie close to portions of the visualized vortex that have undergone deformation, but remain near the wing surface.

The frame 3 (t_{nd} = 6.30) surface pressure topology indicates the outboard end of the suction ridge still terminates near the wing leading edge. However, the inboard end of the ridge has moved downstream and is now located near midchord. Visualization shows the vortex remains at the leading edge near the wingtip, but has begun to convect downstream near the splitter plate. Two local suction peaks are still present near portions of the vortex that appear to have undergone deformation. The inboard peak has moved downstream and is located at 0.44 chord, while the outboard suction peak remains at 0.18 chord. In the ridge central portion, suction magnitude remains depressed, and the vortex arch that appeared in the previous flow visualization frame is still clearly visible. In addition, rotating cells have formed at the juncture where the legs of the vortex arch join the remainder of the vortex. At each location, cell rotation corresponds to that of the vortex, with each cell rotating in a sense opposite the other.

In frame 4 (t_{nd} = 6.96), the surface pressure topology exhibits a suction ridge that begins near the outboard portion of the leading edge and has maximum magnitude there. Visualization is consistent, showing the vortex still anchored to the leading edge near the wingtip. The suction ridge then extends aft and inboard, decreasing in magnitude, and finally terminating near the intersection of the splitter plate and trailing edge. The outboard suction peak is still visible at 0.37 chord, whereas the inboard suction peak no longer exists. Visualization is again consistent, showing the outboard rotational cell near midchord and the inboard one centered over the trailing edge. These two cells are connected by diffuse dye streaks resembling the previously well-defined arch. Finally, a concentration of dye is visible immediately adjacent to the splitter plate. This structure remains connected to the inboard cell by a well-defined dye streak.

The frame 5 (t_{nd} = 7.26) surface pressure topology consists principally of a broad, straight suction ridge extending from the leading edge near the wingtip to the trailing edge near the splitter plate. The outboard suction peak still persists near the wingtip and a new suction peak has formed adjacent to the splitter plate. This new suction peak has substantially lower magnitude than suction peaks observed earlier in the pitch motion, either inboard near the splitter plate or outboard near the wingtip. This is once again consistent with the visualization, which shows the outboard end of the vortex lies close to the wing leading edge. From here the vortex proceeds inboard and aft until it reaches the remaining rotational cell. From the rotational cell, the vortex extends upward and aft before flexing toward the splitter plate and extending inboard. After contacting the splitter plate, the vortex proceeds down toward the wing surface and forward toward the leading edge. It then terminates on the wing surface adjacent to the splitter plate near the new suction peak.

Figure 4 contains three flow visualization photographs showing the leading-edge vortex at chosen intermediate times in the pitch motion for the experimental range of nondimensional pitch rates. These photographs were selected to capture the initial disruptions to the leading-edge vortex gradual arc shape that were precursors to vortex arching. In the visualizations, disruptions appeared as discontinuities in the apparent upstream boundary of the leading-edge vortex. Disruptions subsequently developed into flexure points for the

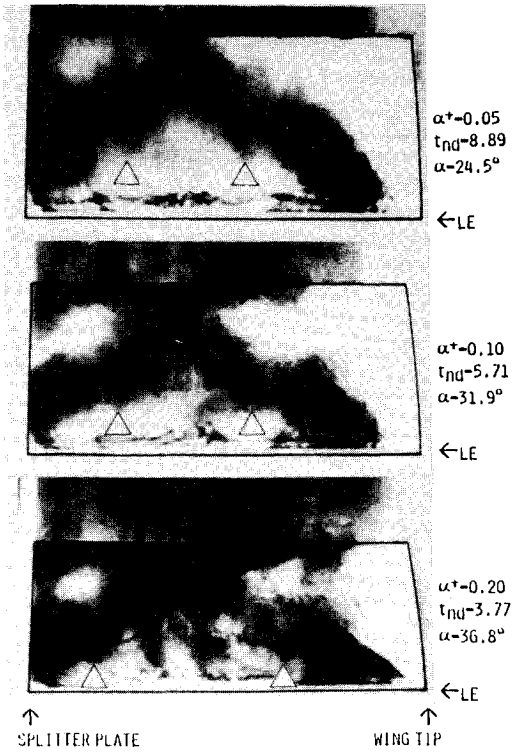

Fig. 4 Flow visualizations of leading-edge vortex at initial disruption for experimental range of α^+ and pitch axis at 0.33*c*.

vortex arch, and then rotational cells. In each photograph, spanwise location of both the inboard and outboard disruptions are marked by arrows. Spatial and temporal relationships between these initial disruptions and the wing are recorded in Table 1.

Table 1 indicates that higher nondimensional pitch rates drive the inboard initial disruption closer to the splitter plate. In addition, higher nondimensional pitch rates force the outboard initial disruption farther from the splitter plate and nearer the tip. When the initial disruptions occur, both inboard and outboard disruptions appear at the same chord location. However, increasing nondimensional pitch rate moves initial occurrence of the disruption farther forward on the wing chord, and delays it to higher angles of attack.

Figure 5 contains three surface pressure contour plots, identical in format to those presented in Fig. 3, for nondimensional pitch rates of 0.05, 0.10, and 0.20. These three contour plots correspond in orientation and scale to the three flow visualization photographs shown in Fig. 4. Thus, these topologies document surface pressure at the time when the leading-edge vortex underwent initial disruption. All three contour plots exhibit a prominent arc-shaped suction ridge that intersects the wing leading-edge inboard near the splitter plate and outboard near the wingtip. Near center span, the suction ridge curves downstream to approximately midchord. Prominent suction peaks are evident on the inboard portion of the suction ridge, located at 0.10, 0.10, and 0.05 span for nondimensional pitch rates of 0.05, 0.10, and 0.20. On the outboard part of the suction ridge, a suction peak is visible at 0.75 span for all three nondimensional pitch rates. Higher nondimensional pitch rates also show denser contour distributions, indicating steeper surface pressure gradients in both the chordwise and spanwise directions at higher nondimensional pitch rates.

Table 1 Spatial and temporal occurrence of initial disruptions shown by visualization in Fig. 4

α^+	Inboard disruption span, y/s	Outboard disruption span, y/s	Both disruptions chord, x/s	Time of disruption occurrence, t_{nd}
0.05	0.25	0.56	0.32	8.89
0.10	0.23	0.57	0.25	5.71
0.20	0.16	0.65	0.18	3.77

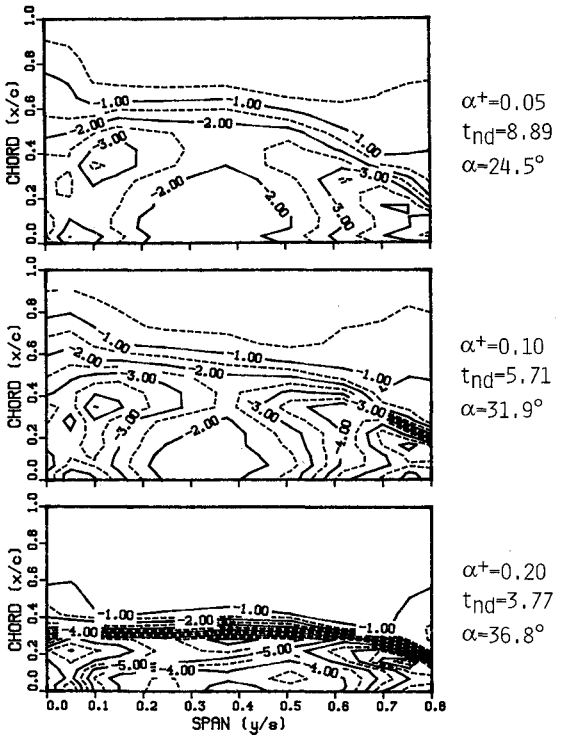

Fig. 5 Surface pressure topologies at initial vortex disruption for experimental range of α^+ and pitch axis at 0.25c.

Leading-Edge Surface Pressure

Figure 6 shows a representative contour plot documenting leading-edge surface pressure coefficient variation with nondimensional time and span location. This plot corresponds to a nondimensional pitch rate of 0.10 and pitch axis location of 0.33 chord. Beginning at nondimensional time 0.0, predominantly two-dimensional suction increase is indicated by the horizontal contours in the lower portion of the plot. However, gradual upward curvature at both the inboard and outboard ends of the contours indicates a lag in suction increase near the wing root and tip. After nondimensional time 4.00, leading-edge suction increase becomes radically nonuniform along the wing span, and three regions are discernible in the plot. In the central region, between 0.15–0.50 span, leading-edge suction first attains a maximum at a nondimensional time of 4.14. Suction subsequently declines at a nearly constant rate as shown by the uniform contour spacing in the vertical direction.

Inboard, between 0.0–0.15 span, the suction peak occurs 0.89 nondimensional time units later than it did in the central region. Suction reaches a local maximum at 0.05 span and nondimensional time 4.80, as indicated by the concentric contours. Following attainment of this maximum, suction decline is slow at first, and then accelerates, as shown by the closer contours after nondimensional time 6.0. Terminal rate of suction decrease is similar for the central and inboard regions of the plot, as evidenced by the comparable distances between adjacent contour lines. The outboard region is dramatically different from both the central and inboard regions. Here, leading-edge suction peaks at 0.80 span and nondimensional time 6.00, nearly 1.50 nondimensional time units after occurrence of the maxima in either the central or inboard region. After reaching this outboard peak, suction decreases at an appreciably slower rate than it did in either the central or inboard region of the plot.

Figure 7 is a summary plot that records the nondimensional time of leading-edge suction maximum at 11 span stations, for the experimental range of nondimensional pitch rate and pitch axis location. Data comprising this graph were extracted from contour plots similar to Fig. 6. Figure 7 shows that leading-edge suction reaches a maximum at earlier nondi-

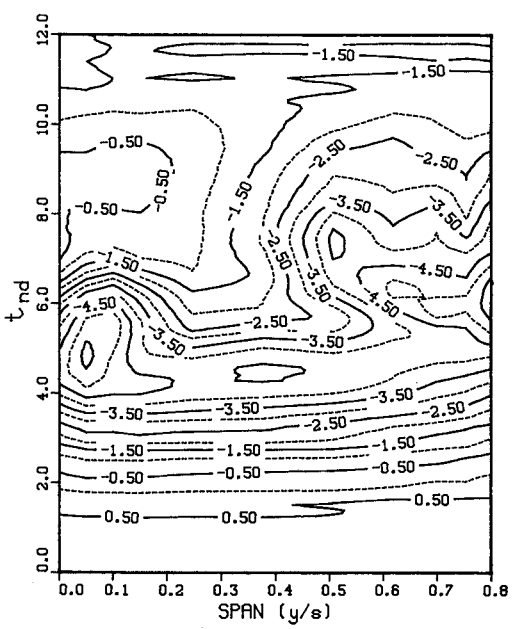

Fig. 6 Representative contour plot of leading-edge c_p vs t_{nd} and span. α^+ = 0.10 and pitch axis is located at 0.33c.

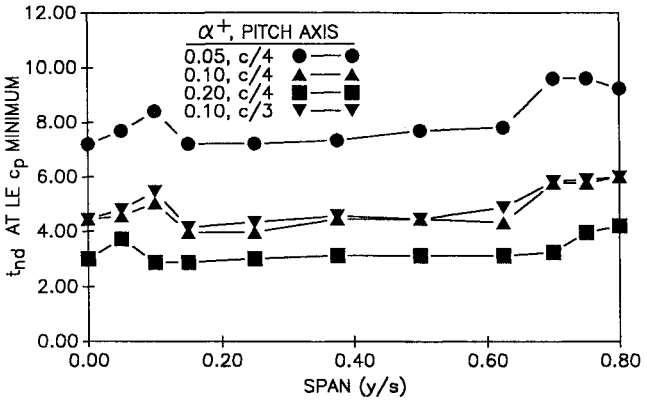

Fig. 7 Summary plot documenting t_{nd} of leading-edge suction collapse vs span for experimental range of α^+.

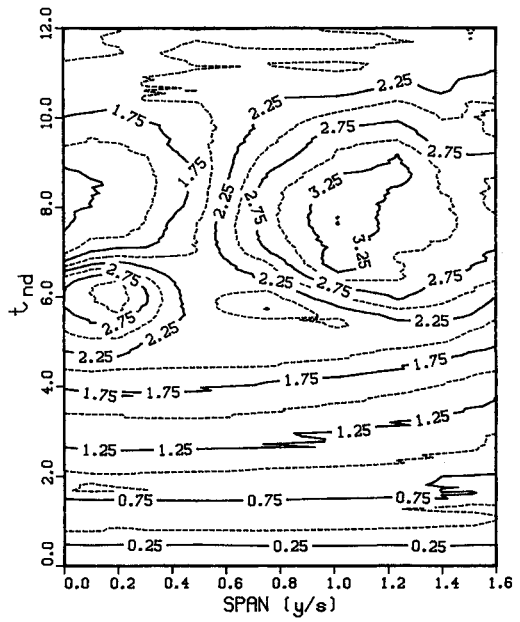

Fig. 8 Contour plot C_n vs t_{nd} and span. $\alpha^+ = 0.10$ and pitch axis is located at 0.33c.

mensional times for higher nondimensional pitch rates, corresponding to higher instantaneous angles of attack. Moving the pitch axis from 0.25 to 0.33 chord for nondimensional pitch rate 0.10 also imposes a slight delay upon leading-edge suction peak occurrence.

All four plots in Fig. 7 are dominated by a broad, level central region. This portion of the curve shows that leading-edge suction maxima occurred first, and nearly simultaneously, over the central portion of the wing span for each nondimensional pitch rate. Inboard and outboard of these level regions, all four curves bend sharply upward. This indicates significant delays in the attainment of leading-edge suction maxima near both splitter plate and wingtip. All four plots show suction maxima occurring first in the broad central region of the wing span, followed by maxima inboard near the splitter plate and, finally, outboard near the wingtip. Higher nondimensional pitch rates generally drove the spanwise locations of suction maximum delay closer to the splitter plate and wingtip.

Spanwise Normal Force Loading

Figure 8 is a representative contour plot showing normal force coefficient variation with nondimensional time and span location. Normal force initially increases uniformly across the wing span with nondimensional time as shown by the horizontal contours. However, at nondimensional time 2.0, the contours at the outboard span stations begin to curve upward and are spaced farther apart, indicating a reduced rate of normal force increase there. At nondimensional time 5.0, similar upward curvature and reduced contour density occurs at the inboard span stations, also indicating reduced rates of normal force increase near the splitter plate. Prior to nondimensional time 5.0, normal force variation remained highly uniform across the span, in spite of the minor perturbations noted above.

After nondimensional time 5.0, spanwise variation in normal force suffered severe three-dimensional disruption. Figure 8 exhibits a pronounced inboard normal force maximum of 2.95, as evidenced by the concentric contours centered at 0.1 span and nondimensional time 5.94. A similar normal force maximum of larger spatial and temporal extent, and magnitude 3.50, occurs outboard as indicated by the concentric contours centered at 0.5 span and nondimensional time 7.62. Between these two regions on the plot, from approximately 0.2 to 0.4 span, lies an area characterized by sparse contours of significantly lower magnitude. In this central region, normal force stalls at nondimensional time 5.58 and attains a maximum value of 2.16. Normal force then declines more slowly than it does either inboard near the splitter plate or outboard in the tip region.

At nondimensional time 8.0, normal force coefficient decreased to a minimum of approximately 1.25 at 0.0 span, and simultaneously increased to a maximum of 3.75 at 0.5 span. Between these two span locations, at 0.25 span, a region of nearly vertical contours indicates negligible temporal change in normal force. Subsequently, normal force increased inboard, decreased outboard, and underwent little change in the vicinity of 0.25 span. At nondimensional time 11.0, normal force became uniform across the span at a magnitude of approximately 2.0.

Figure 9 is a summary plot containing information extracted from contour plots similar to Fig. 8. Figure 9 records the nondimensional time of normal force maximum, or normal force stall, at 11 span stations for the experimental range of nondimensional pitch rate and pitch axis location. Figure 9 shows that at any given span station normal force stall occurs at earlier nondimensional times for higher nondimensional pitch rates, corresponding to higher instantaneous angles of attack. For nondimensional pitch rate 0.10, moving the pitch axis from 0.25 to 0.33 chord slightly delayed normal force stall.

All four curves in Fig. 9 show similar spanwise stall progressions. Normal force stall occurred first at 0.375 span for nondimensional pitch rate 0.20, and at 0.25 span for the remaining three conditions. Stall occurred next inboard, near the splitter plate. Here, inboard of 0.25 span, stall occurred last at 0.10 span for nondimensional pitch rate 0.05, and at 0.05 span for the other three conditions. Finally, normal force stalled outboard, near the wingtip. The spanwise location of final stall moved inboard with higher nondimensional pitch

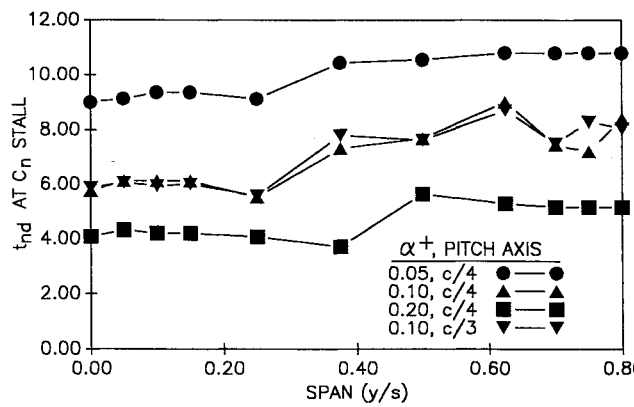

Fig. 9 Summary plot showing t_{nd} of C_n stall vs span for experimental range of α^+.

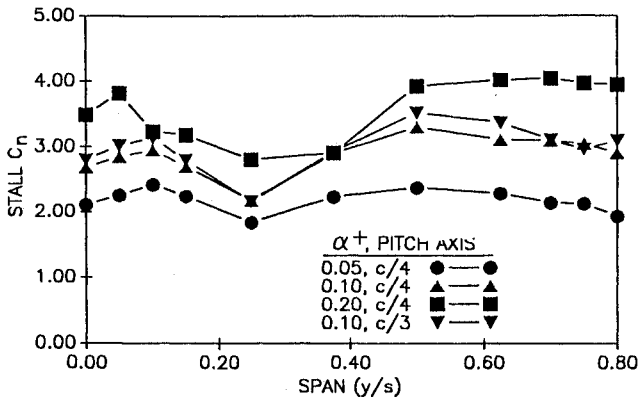

Fig. 10 Summary plot of stall C_n vs span for experimental range of α^+.

rate, progressing from 0.70 to 0.625 span, and finally to 0.50 span for nondimensional pitch rates of 0.05, 0.10, and 0.20.

Figure 10 summarizes data taken from contour plots like Fig. 8, and documents stall normal force coefficient at 11 span stations for the experimental range of nondimensional pitch rate and pitch axis location. Figure 10 shows that, at any given span station, stall normal force coefficient increases with higher nondimensional pitch rate. For nondimensional pitch rate 0.10, moving the pitch axis from 0.25 to 0.33 chord generally increases stall normal force slightly.

Again, all four curves in Fig. 10 display similar trends. Stall normal force was lowest at 0.25 span for all four conditions. For each of the four curves, absolute maxima of stall normal force generally occurred outboard near the wingtip. Such absolute maxima occurred at 0.70 and 0.50 span for nondimensional pitch rates of 0.20 and 0.10. However, for nondimensional pitch rate 0.05, stall normal force reached absolute maximum at 0.10 span. In addition to the absolute maxima, local maxima also occurred at the opposite end of the span. Local maxima occurred at 0.10 span for nondimensional pitch rates 0.05 and 0.10, and at 0.05 span for nondimensional pitch rate 0.20.

Discussion

Flow visualization, surface pressure topologies, and spanwise normal force loading histories provided diverse information regarding the unsteady flow over the pitching wing-splitter plate configuration. Correlating these data enabled formulation of a cohesive account of vortex kinematics, underlying vorticity dynamics and spanwise normal force loading.

Temporal and spatial fluctuations of considerable magnitude were observed in flow visualization, surface pressure topologies, and spanwise normal force loading histories. In contrast, Fig. 2 showed that the rigid wing-splitter plate combination pitched at constant rate in uninterrupted fashion. Thus, kinematic or geometric anomalies did not contribute to these prominent temporal and spatial variations.

Dye flow visualization revealed a large, energetic leading-edge vortex that persisted during a significant interval of the pitch motion and extended over a large area of the wing planform. Following initiation near the wing leading edge, the vortex convected downstream toward the wing trailing edge while growing in cross section. Vortex growth and convection were accompanied by radical three-dimensional deformation. Visualized vortex structures and locations were corroborated by prominent pressure minima that dominated surface pressure topologies, consistent with observations made by Walker and colleagues[14] for surface pressure distributions on two-dimensional airfoils. Modifications to vortex structure or location were accompanied by corresponding alterations to surface pressure topologies.

Soon after a predominantly two-dimensional initiation, Fig. 3 (frame 1, t_{nd} = 5.28) showed that the leading-edge vortex had experienced limited convection near the splitter plate and wingtip. Here, pressure minima occurred in the surface pressure contours consistent with enhanced vortex-surface interaction due to vorticity straining. The central portion of the vortex had convected downstream, forming a moderate vortex arc lying near the wing surface. This limited three dimensionality was reflected in the Fig. 8 normal force contour plot as a mild disruption to the previously two-dimensional contour lines.

The gradual vortex arc was initially disrupted as visualized in Fig. 4, and confirmed by surface pressure contours in Fig. 5. Initial vortex disruptions moved farther apart, and closer to both splitter plate and wingtip, with higher nondimensional pitch rate. The two delayed leading-edge suction maxima of Fig. 7 also moved apart, shifting the inboard one closer to the splitter plate, and the outboard one closer to the wingtip as nondimensional pitch rate increased. Comparing Table 1 to Fig. 7 showed that leading-edge suction collapse preceded initial vortex disruption by approximately 1.0–2.0 nondimensional time units, and that this intervening period shortened with higher nondimensional pitch rate. Table 1 also showed that the vortex was located closer to the wing leading edge at initial disruption with increasing nondimensional pitch rate.

These correlations indicate that leading-edge suction collapse indicated the demise of pressure gradients responsible for vorticity production. Vorticity production curtailment, in turn, disrupted the vorticity sheet feeding the downstream leading-edge vortex. Acharya and Metwally[16] have shown that disruption of vorticity production in the leading-edge region imposes pronounced modifications upon leading-edge vortex kinematics downstream.

That portion of the vortex between the two initial vortex disruptions subsequently arched over the wing surface as visualized in Fig. 3 (frame 2, t_{nd} = 5.88). Vortex arching kinematics in the current investigation were consistent with those visualized by Schreck et al.,[11] Freymuth,[4] and Horner et al.[10] Vortex arching was accompanied by suction collapse on the wing area vacated by the vortex. Here, vortex-surface separation distance increased, reducing vortex-surface interaction and attenuating suction as demonstrated by Panaras.[15]

Following vortex arching, the apex of the arch convected downstream at a significantly higher speed than the remainder of the vortex. Vortex convection velocity was locally accelerated when the arched portion of the vortex encountered stronger freestream influence.[10,20] However, vortex arch height above the wing prevented vortex convection from strongly impacting either surface pressures or normal forces.[15] This was indicated by the sparse and then vertical contours immediately inboard of center span in Fig. 8. Vorticity straining in the remainder of the vortex was augmented by the vortex arch and continued to amplify vortex-surface interaction, both near the splitter plate and the wingtip. This, in turn, prompted corresponding maxima in surface pressure topologies and spanwise normal force loading topologies.

At the two sites where the vortex flexed to accommodate arching, counter-rotating cells appeared at the wing surface, as visualized in Fig. 3 (frame 3, t_{nd} = 6.30). Initially, these cells were symmetric in the spanwise direction about a line just inboard of the wing center span. Similar cell pairs have been observed under dynamic conditions by Shih,[9] Schreck,[17] and Horner et al.,[10] and in the static regime by Winkelmann and Barlow.[18] Rotational sense of the cells was consistent with that of the contiguous leading-edge vortex that had arched up over the wing surface. At this time, the leading-edge vortex near the splitter plate began to convect away from the leading edge, locally deforming the vortex. Figure 8 showed approximately equal values of normal force inboard and outboard. However, normal force had peaked and was decreasing inboard near the splitter plate while continuing to increase outboard near the wingtip.

After the symmetric pair of counter-rotating cells appeared, these cells and the associated vortex convected asymmetri-

cally. Figure 3 (frame 4, $t_{nd} = 6.96$) showed that the inboard cell reached the trailing edge well in advance of the outboard one, even though both began at the same chord location. This observation is consistent with observations made by Schreck et al.[11] who observed accelerated vortex convection near the wing-splitter plate juncture. Inboard, vortex convection began shortly after leading-edge suction finally collapsed near the splitter plate, as recorded in Fig. 7. The influence of asymmetric convection was consistent with normal force stall times shown in Fig. 9, which showed that normal force stall occurred inboard significantly earlier than it did at outboard span stations. Asymmetric vortex convection was prompted by a combination of influences. Outboard, near the wingtip, vortex convection was retarded by pinning at the tip region as visualized by Freymuth,[4] and quantitatively corroborated by Robinson and coworkers.[8] Inboard, vortex convection was accelerated by mutual induction acting between the inboard leg of the vortex arch and the vortex image presented by the splitter plate.

Finally, Fig. 3 (frame 5, $t_{nd} = 7.26$) showed the outboard portion of the leading-edge vortex began to convect downstream and away from the leading edge near the wingtip. Soon after this time Fig. 8 showed normal force reaching a maximum near the wingtip and beginning to decline. Experiments by Lorber et al.[19] have recorded similar lift maxima restricted to the wingtip region. Inboard, visualization showed the vortex above and behind the wing surface, but still apparently connected to the wing surface by two vortex segments emanating from the wing surface. By this time, the inboard portion of the wing had stalled and nearly reached minimum normal force.

Figure 7 showed that leading-edge suction collapse, near both the splitter plate and wingtip, was significantly delayed relative to central span locations. Outboard, downwash produced by the prominent wingtip vortex delayed leading-edge suction collapse compared to center span. Similar delays in leading-edge suction collapse inboard suggest a concentration of streamwise vorticity, of opposite sense to that at the wingtip, is also present near the wing-splitter plate juncture.

Surface pressure gradients on the wing-splitter plate configuration gave rise to localized concentrations of streamwise vorticity. Low pressures produced on the wing during pitching would induce secondary flows over the splitter plate toward the wing. Thus, streamwise vorticity would be generated and convected over the splitter plate toward the wing, collecting in the wing-splitter plate juncture. Although no streamwise vortex was observed in the juncture region, a concentration of streamwise vorticity not coalesced into a vortex would also induce downwash and preserve leading-edge suction. Juncture vortices have been visualized by Klinge et al.[12] near the juncture of a pitching wing-splitter plate configuration.

The amount of streamwise vorticity present at either the wingtip or the juncture dictated the influence that it exercised. In Fig. 7, leading-edge suction collapse delays were longer and extended farther inboard from the wingtip than delays near the splitter plate. This asymmetry suggests that larger amounts of streamwise vorticity were present near the wingtip than at the juncture at leading-edge suction collapse. Figure 7 also showed that leading-edge suction collapse delay was displaced closer to the wingtip and juncture with increasing nondimensional pitch rate. This is consistent with the model proposed by Luttges and Kennedy,[20] wherein higher nondimensional pitch rates reduce total vorticity production and prompt more condensed vorticity distributions.

Conclusions

A generic wing-splitter plate configuration was pitched at constant rate to angles exceeding the static stall angle. The resulting three-dimensional unsteady flowfield was characterized using dye flow visualization and unsteady surface pressure measurements. Visualized three-dimensional deformations of the leading-edge vortex were corroborated by complex surface pressure topologies that were similarly three-dimensional in nature. Spanwise variations in normal force loading were consistent with three-dimensional vortex deformations. Mechanisms based upon vorticity dynamics were postulated to account for these observed kinematics.

The initially two-dimensional unsteady vortex rapidly underwent three-dimensional deformation along the entire wing span. Three-dimensional deformation began when vortex convection was arrested near the splitter plate and wingtip, but continued near center span. Soon, disruptions appeared in the vortex upstream boundary, and were quickly followed by vortex arching above the wing surface near center span. Subsequently, vortex convection near the splitter plate outpaced that near the tip, with the inboard portion of the vortex being shed prior to that outboard.

Vortex kinematics were driven by an identifiable set of vorticity dynamics. Streamwise vorticity accumulated near the splitter plate and wingtip. These vorticity accumulations temporarily arrested vortex convection and delayed vortex arching. Mutual induction acting between the vortex arch and the image of it presented by the splitter plate accelerated vortex convection near the splitter plate.

Spanwise normal force loading was consistent with vortex kinematics. Two-dimensional and moderately three-dimensional vortex structure yielded normal force loading that was uniform along the span. Prominently three-dimensional vortex structure prompted correspondingly nonuniform spanwise normal force loading. Normal force stall times varied substantially across the span, and were closely correlated to vortex arching or shedding.

This experiment has examined three-dimensional dynamically separated flow over a generic wing-splitter plate configuration. Many aspects of this flow have been successfully characterized and explained, though only for a limited parameter range. As such, the current investigation provides a basis for further investigations employing configurations of more practical interest and encompassing broader parameter ranges.

Acknowledgments

The authors would like to express their gratitude to Marvin Luttges and Michael Robinson, University of Colorado at Boulder, for many helpful discussions and suggestions.

References

[1]Adler, J., and Luttges, M., "Three-Dimensionality in Unsteady Flow About a Wing," AIAA Paper 85-0132, Jan. 1985.

[2]Ashworth, J., and Luttges, M., "Comparisons in Three-Dimensionality in the Unsteady Flows Elicited by Straight and Swept Wings," AIAA Paper 86-2280, Aug. 1986.

[3]Robinson, M., Helin, H., Gilliam, F., Russell, J., and Walker, J., "Visualization of Three-Dimensional Forced Unsteady Separated Flow," AIAA Paper 86-1066, May 1986.

[4]Freymuth, P., Finaish, F., and Bank, W., "Three-Dimensional Vortex Systems of Finite Wings," *Journal of Aircraft*, Vol. 25, No. 10, 1988, pp. 971, 972.

[5]Freymuth, P., "Visualizing the Connectivity of Vortex Systems for Pitching Wings," *Journal of Fluids Engineering*, Vol. 111, June 1989, pp. 217–219.

[6]Gad-el-Hak, M., and Ho, C.-M., "Three-Dimensional Effects on a Pitching Lifting Surface," AIAA Paper 85-0041, Jan. 1985.

[7]Lorber, P. F., "Tip Vortex, Stall Vortex, and Separation Observations on Pitching Three-Dimensional Wings," AIAA Paper 93-2972, July 1993.

[8]Robinson, M., Walker, J., and Wissler, J., "Unsteady Surface Pressure Measurements on a Pitching Rectangular Wing," *Proceedings of Workshop II on Unsteady Separated Flow*, U.S. Air Force Academy, Colorado Springs, CO, 1988, pp. 225–237.

[9]Shih, C., "Unsteady Aerodynamics of a Stationary Airfoil in a Periodically Varying Freestream," Ph.D. Dissertation, Univ. of Southern California, Los Angeles, CA, 1988.

[10]Horner, M., Addington, G., Young, J., and Luttges, M., "Controlled Three-Dimensionality in Unsteady Separated Flows About a Sinusoidally Oscillating Flat Plate," AIAA Paper 90-0689, Jan. 1990.

[11]Schreck, S., Addington, G., and Luttges, M., "Flow Field Structure and Development Near the Root of a Straight Wing Pitching at Constant Rate," AIAA Paper 91-1793, June 1991.

[12]Klinge, J., Schreck, S., Robinson, M., and Luttges, M., "Three-Dimensional Flow Field Kinematics near the Root of an Oscillating Wing," AIAA Paper 91-3264, Sept. 1991.

[13]Schlichting, H., *Boundary Layer Theory*, 7th ed., McGraw-Hill, New York, 1979, p. 383.

[14]Walker, J., Helin, H., and Chou, D., "Unsteady Surface Pressure Measurements on a Pitching Airfoil," AIAA Paper 85-0532, March 1985.

[15]Panaras, A., "Numerical Modeling of the Vortex/Airfoil Interaction," *AIAA Journal*, Vol. 25, No. 1, 1987, pp. 5–11.

[16]Acharya, M., and Metwally, M., "Evolution of the Unsteady Pressure Field and Vorticity Production at the Surface of a Pitching Airfoil," AIAA Paper 90-1472, June 1990.

[17]Schreck, S. J., "Experimental Investigation of the Mechanisms Underlying Vortex Kinematics in Unsteady Separated Flows," Ph.D. Dissertation, Univ. of Colorado, Boulder, CO, 1989.

[18]Winkelmann, H., and Barlow, J., "Flowfield Model for a Rectangular Planform Wing Beyond Stall," *AIAA Journal*, Vol. 18, No. 8, 1980, pp. 1006–1008.

[19]Lorber, P., Covino, A., and Carta, F., "Dynamic Stall Experiments on a Swept Three-Dimensional Wing in Compressible Flow," AIAA Paper 91-1795, June 1991.

[20]Luttges, M., and Kennedy, D., "Initiation and Use of Three-Dimensional Unsteady Separated Flows," *Proceedings of Workshop II on Unsteady Separated Flow*, U.S. Air Force Academy, Colorado Springs, CO, 1988, pp. 211–222.